Chapter 12

Semiconductor THz Lasers and Their Applications in Spectroscopy of Explosives

Mykhailo Klymenko, Oleksiy V. Shulika and Igor A. Sukhoivanov

Additional information is available at the end of the chapter

http://dx.doi.org/10.5772/67625

Abstract

Recently, applications of THz spectroscopy for detecting explosive agents have attracted much attention due to following reasons: many CBRNE agents have fingerprint-like features in the THz wavelength range; the THz spectroscopy provides an ability for remote and non-destructive identification of explosives; the THz radiation penetrates through many covering dielectric materials including paper, leather, fabric and so on. One of the most important components of THz spectroscopy setups is the source of THz radiation, which has to be high-power, tunable, low-cost and to have compact sizes. In this chapter, we are going to overview recent progress of wide variety of THz emitters considered as candidates for that role. We will pay a special attention to recent trends in engineering of spectral characteristics of THz quantum-cascade lasers and their tunability. Also we will describe the advantages and difficulties that accompany a THz spectroscopy of explosives.

Keywords: terahertz time-domain spectroscopy, quantum-cascade laser, photoconductive antenna, CBRNE agents, gain spectrum

1. Introduction

The term CBRNE is an acronym for chemical, biological, radiological, nuclear, and explosive agents that represent warfare hazards [1]. The terahertz spectroscopy in the range 0.1–10 THz has become an important tool for studying the low frequency vibrational properties of molecules in the condensed phase. Many CBRNE agents exhibit characteristic spectral features in the THz frequency range, mainly in 0.5–10 THz [2, 3]. Therefore, THz spectroscopy has shown strong potential for security applications related to the detection of CBRNE materials [4, 5].

Additionally, in recent years, there has been significant progress in imaging of metallic objects under dielectric covering materials by using the millimeter wave/lower THz frequency range 50 GHz – 1 THz [6]; many imaging techniques have already found their applications in UK airports [7]. Both active and passive imaging modalities have been proposed; the former involves the analysis of radiation directed at the target by an operator, while the latter relies on naturally occurring ambient radiation emitted by, or reflected off, the target.

One of main advantages of THz spectroscopy and imaging is based on the fact that many dielectric materials such as paper, leather and woven, cotton and synthetic fabric are transparent in THz frequency range. Differences in the electromagnetic properties of skin, explosives, metal and so on can allow the detection of weapons or concealed packages. Another advantage of the THz frequency radiation is that it has a relatively low photon energy and, thus, it is nonionizing in comparison with X-rays that makes it potentially more suitable for human-involved scanning and detections. Furthermore, the radiation power obtainable from typical THz-TDS systems is rather small (less than 1 mW) and is not considered to pose a health risk [8], although QCL pulse and CW sources, which can be characterized by the radiation power greater than tens of milliwatts, may pose some risks for operators and personnels.

The most widely used THz-based technique for the spectroscopic identification of CBRNE agents is based on the THz time domain spectroscopy (THz-TDS). One of the most important components of THz spectroscopy setups is a source of radiation which has to be high-power, tunable, and low-cost having compact sizes. In Section 2, we are going to review a recent progress of wide verity of semiconductor THz lasers considered as candidates for that role. We will pay special attention on the recent trends in the tunability of THz quantum-cascade lasers. In Section 3, we will describe a basic THz-TDS setup and its application in spectroscopy of CBRNE.

2. THz emitters

2.1. Variety of THz sources

According to Tonouchi's review paper [9], THz sources can be classified into three categories: THz sources based on the emission induced by an optical radiation, quantum-cascade lasers, and sources based on solid-state electronic devices. The first category includes devices that involves generating ultrafast photocurrents in a photoconductive antenna [10, 11] with the carrier acceleration by the external electric-field, by the surface-depletion field, or by means of the photo-Dember effect in semiconductors [12]. This category also includes devices whose operation is based on non-linear optical effects induced by an incident CW optical radiation (optical rectification, difference-frequency generation, and optical parametric oscillations). The second category covers devices based on semiconductor quantum-cascade structures where THz radiation results from the drift electrical current passing through a multi-layered electrically-biased semiconductor structure. The third category includes devices such as uni-travelling-carrier photodiodes and Gunn diodes. In this chapter, we focus on the first two categories of devices which are the most suitable for the THz time-domain spectroscopy. Also, we shrink variety of considered devices to

those based on semiconductor materials only. For instance, we exclude from the overview pretty efficient THz emitters based on an optically excited plasma in atmosphere [13] which allow to provide remote spectroscopic measurements for distant objects. Moreover, we do not aim to provide a comprehensive overview of all aspects of those THz generators but rather focus on the properties related to applications in the THz spectroscopy and chemical sensing.

2.2. Photoconductive antennas

One of the most common ways to generate THz radiation exploits semiconductor photoconductive antennas made of semiconductor materials and metallic stripes decomposed on its surface. Exposed to light with the photon energy overcoming the band gap of the semiconductor, the active region of the photoconductive antenna changes its electrical conductivity due to optically generated electron-hole pairs under the surface (see **Figure 1**). The free charge carriers are accelerated by the electrostatic field created by metallic stripes. The most commonly used materials for THz photoconductive antennas are radiation-damaged silicon-on-sapphire and low-temperature grown GaAs. The materials are such that their carrier lifetimes are in the subpicosecond range. The short lifetimes are determined by a high concentration of defects, at which carriers are trapped and recombined. The defects are caused by O^+ ions implanted in silicon by the ion bombardment [14]. The density of defects is controlled by the intensity of and timing of the ion beam. The low-temperature grown gallium arsenide is grown by molecular beam epitaxy at low substrate temperatures with followed rapid thermal annealing. The material contains a high density (>1018 cm^3) of point defects such as As antisites, As interstitials, and Ga-related vacancies [15]. The effective carrier mobilities of radiation-damaged silicon-on-sapphire and low-temperature grown GaAs are reported as 10–100 cm^2/V s [16] and 200–400 cm^2/V s, respectively [17]. Since the mobility of holes in low-temperature grown GaAs is lower by an order of magnitude than the mobility of electrons, carrier transport in the THz frequency range is dominated by electrons.

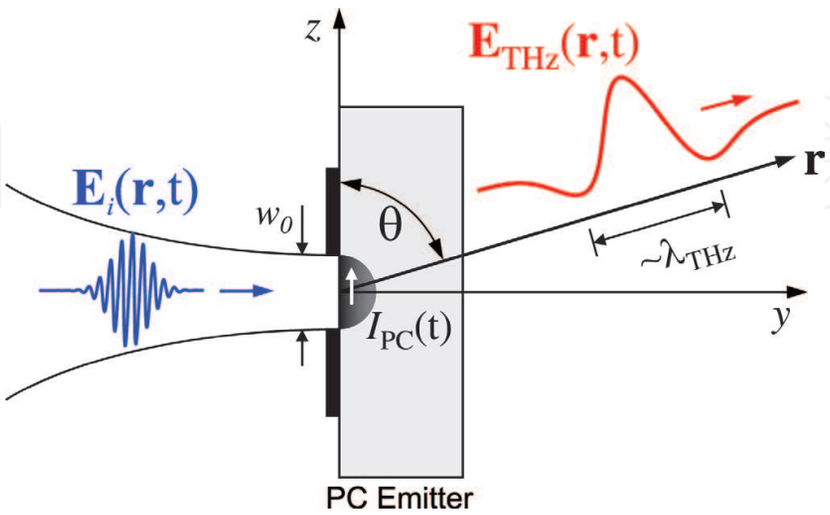

Figure 1. Generating THz radiation from the photoconductive antenna (adopted from [10]).

The output power of a photoconductive emitter depends on the bias voltage and the optical pump power. The amplitude of the radiation field increases with both parameters [11]. The maximum radiation power, however, is limited by the breakdown voltage of its substrate material. The breakdown field of the low-temperature grown GaAs is reported as ~300 kV/cm. The THz output power saturates at high optical pump powers due to the screening of the bias field by photocarriers. This saturation effect is more pronounced in dipole antennas comparing to other types of antennas. This is caused by the small size of the gap between electrodes in the dipole antennas. Nowadays, the output power of the commercial available photoconductive emitters is limited by tens of microwatts in the pulse operating mode [18, 19].

The photoconductive antennas are broadband (with the bandwidth of several THz [20]) that is beneficial for the THz time-domain spectroscopy.

The photoconductive emitters may exploit nonlinear optical effects as well. In this case, the optical radiation interacts with the non-linear medium of a semiconductor material generating THz radiation. Several non-linear effects may be employed: the optical rectification, which is a second-order non-linear processes [12], and photomixing (see Ref. [10] for instance). Such methods of THz emission allow for the continuous-wave generation; however, the emission power of such type of emitters is not large enough for most of the spectroscopic applications.

In principle, even a pure surface of a bulk semiconductor material without metallic stripes and applied external electrostatic fields can radiate terahertz radiation after being excited by an ultra-fast optical pulse. In this case, photo-generated carriers are accelerated by means of the surface depletion layer electric field or photo-Dember effect [21]. The photo-Dember effect is related to spikes of a photocurrent that arises as a result of the difference between diffusion velocities of electrons and holes. Because electrons respond to applied electric field with a larger acceleration due to their higher mobility comparing to holes, electrons diffuse more rapidly from the surface inside the semiconductor material. That creates an effective surge current normal to the surface. Although the emission of THz radiation from pure semiconductor surfaces represents an interest as a diagnostic tool for semiconductor surface physics, it is not widely exploited in applications due to its extremely low output power.

2.3. Quantum-cascade lasers

The photoconductive antennas are pretty bulk devices containing the generator of ultra-shot optical pulses as their integral part. Also, they are characterized by low converting efficiency. A good candidate to overcome these problems is the quantum-cascade structure, a compact electrically driven THz source operating in both pulse and cw mode. QCLs are unipolar devices where a laser emission is achieved through a series of the intersubband transitions in a repeated stack of semiconductor multiple quantum-well heterostructures. The idea of such heterostructures was first proposed by Kazarinov and Suris in 1971 [22], and later implemented for the mid-infrared radiation by Jerome Faist, Federico Capasso, Deborah Sivco, Carlo Sirtori, Albert Hutchinson, and Alfred Cho at Bell Laboratories in 1994 [23].

Band diagrams, band structures, and joint density of states for both interband and intersubband quantum-well devices are schematically shown in **Figure 2**. In the interband structures,

http://dx.doi.org/10.5772/67625

the optical radiation is a result of electron transitions from the conduction subband to the valence subband. As a result, the minimal quantum of the energy is limited by the band gap of the quantum-well material. Curvatures of the bands involved in the transition have very different magnitudes and, what is more important, different senses of curvature. It results in the joint density of states, which is step one in this case.

Optical transitions in the quantum-cascade heterostructures occur between subbands within an allowed band (see **Figure 2(b)**). In contrast to the energy gap between two bands, the subband structure is governed by the conduction band offset and width of the quantum-well layer. Minimal transition energy is not limited by the fundamental band gap and can be tailored by a material composition of the quantum well and the thickness of the quantum-well layer. Since there is no a fundamental limit exposed on the energy gap between two subbands, the intersubband transitions may be exploited to achieve lasing in THz range. The curvature of dispersion curves characterized by the effective masses is usually almost the same for all subbands. It results in the joint density of states being localized around a constant transition energy E_{12}, **Figure 2(b)**. Such a joint density of states results in narrow-band optical characteristics of QCLs which are farther shrunk due to the cavity effect.

A single cascade of QCL usually consists of two parts: the active region and the injector (see **Figure 3**). The radiative intersubband transitions occur in the active region, while the injector serves to extract electrons from the lowest subband in a cascade of QCL and to transfer them to the upper subband in the next cascade providing thus the electron pumping on the upper laser levels. Also, another role of the injector is to block leakage of electrons from the upper subband to the next cascade.

There are generally two different approaches adopted for the injector of terahertz QCLs: chirped superlattice [24] and resonant phonon depopulation [25]. The chirped superlattice is based on fast intraminiband scattering that is engineered in a way to achieve a population inversion between two minibands. This approach shows the lowest threshold current density. The resonant-phonon design relies on fast resonant electron-phonon scatterings which serve to provide an electron extraction from one cascade to another (see **Figure 3**). Because of the relatively large phonon energy of 36 meV compared to the superlattice miniband width of

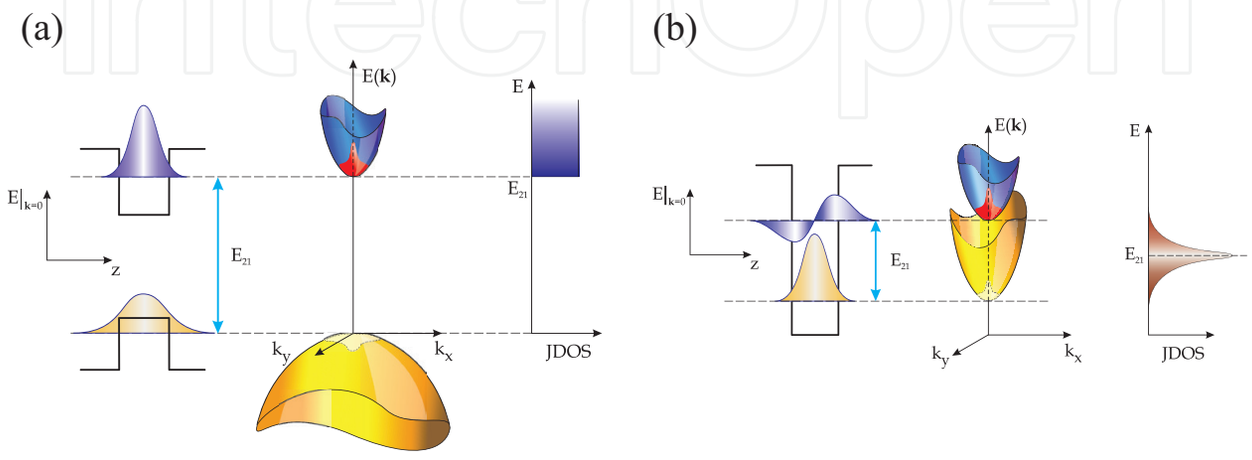

Figure 2. (a) Interband and (b) intersubband radiative transitions in semiconductor quantum-well structures.

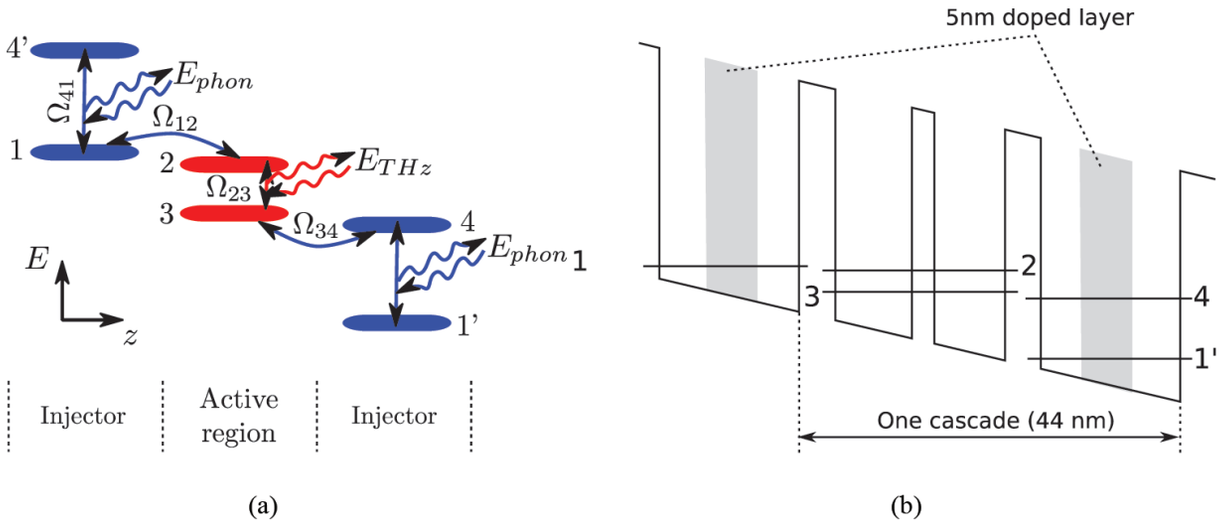

Figure 3. (a) Energy versus coordinate structure of the subband edges in the three-well QCL and (b) the energy diagram of the three-well QCL reported in [31]: the layer thicknesses are of 43/89/24.6/81.5/41/160 angstroms starting from injector barrier (the barriers are indicated in bold fonts). The electrical bias equal 12.2 kV/cm.

15 meV , the resonant-phonon design has less thermal backfilling, and an enhancement in operating temperature has been demonstrated [25]. In the first resonant-phonon design, one cascade of the structure consisted of four quantum wells: two wells to form the pair of lasing states (active region) and two wells for the phonon depopulation and carrier injection (these wells are often called the phonon and injector wells, respectively). That QCL was able to operate in both pulse regime [26] and cw mode [27]. It has been lately optimized to enhance the maximum operating temperature from 137 to 164 K for the pulse mode and from 93 to 117 K in cw mode [28].

In a simpler case, the phonon and the injector wells may be combined [29]. When the design with a single quantum well per injector was first proposed [23], it has slightly less maximum operating temperature of 142 K in pulse mode with the lasing frequency of 3.4 THz. However lately [30], the three-well design has been optimized and it has been proven that this design combines simplicity with a good performance (at the lasing frequency of 3.9 THz, 63 mW of peak optical power was measured at 5 K, and approximately 5 mW could still be detected at 180 K). The most recent advances on the three-well design has been reported in Ref. [31] and reviewed inRef. [32]. According to Ref. [31], the new temperature record for the three-well QCL is 199.5 K with lasing frequency of 3.22 THz and detectable output power. The structure may operate also at 8 K with the emission power of approximately 38 mW and a threshold current density of 1 kA/cm^2.

Below we describe the design of the three-well QCL showing a record operating temperature reported in [31]. Although terahertz QCLs based on InGaAs/InAlAs have been demonstrated [33], the majority of THz QCLs reported are made from GaAs/AlGaAs system because of its flexibility in barrier height that offers an additional degree of freedom for designing. The design is based on the GaAs/$Al_{0.15}Ga_{0.85}As$ material system. The laser structure was grown by molecular beam epitaxy on a semi-insulating GaAs substrate with a 10 μm-thick active region and a sheet electron density of 3 × 10^{10} cm^{-2} per period using a 3D Si-doping within

the middle 5 nm of the injector well. The active region is placed between 100 nm bottom n+ GaAs layer, doped with impurity concentration of 5×10^{18} cm^{-3}, and a top stack consisting of 50 nm of 5×10^{18} cm^{-3} and 10 nm of low temperature-grown 5×10^{19} cm^{-3} n+ GaAs layers. The wafers were first processed into THz QCL structures with Au double metal with wide top Ti/Au metallization forming a Schottky contact, and 1 mm-long Fabry-Perot resonator. In this configuration, the device was lasing with the maximal temperature of 180 K. Additional enhancing of the maximal operating temperature has been achieved by lowering the waveguide loss and improving heat dissipation. That has been achieved by using Cu-Cu-based process with lower waveguide loss and better heat dissipation. Also, the 100 nm thick top n+ contact layer was removed that has further lowered the waveguide loss. The waveguide of the THz QCLs is based on a Cu-Cu double metal geometry. It was fabricated by using Cu-Cu wafer bonding and standard photolithography. Such a metal waveguide provides a large confinement factor close to unity; however, it has relatively high losses caused by the free-carrier absorption. The contacts are represented by bottom and top metal stacks: the first one is made of Ta/Cu (10/600 nm) and the second one is made of Ta/Cu/Ti/Au (10/300/20/150 nm). Wet etching was performed ($H_3PO_4/H_2O_2/H_2$:3/1/25) to etch through the entire thickness of the 10 μm-thick active region. The ridge waveguide of fabricated THz QCLs is ~170 μm wide. The substrate of the samples was thinned down to ~150 μm [31] and then cleaved into laser bars with a 1.8 mm-long Fabry-Perot resonator. The laser bars were then gold plated on the backside, indium soldered on a copper package, and then mounted in a closed-cycle cryostat for measurements [31].

At the electrical bias of 12.2 kV/cm, each cascade of QCL has four subbands with following energy gaps between their edges: E_{23} = 11.5 meV, E_{13} = 14.2 meV, and $E_{41'}$ = 34.6 meV (see **Figure 3(b)** to understand subband numbering). The lasing occurs between subbands 2 and 3. The injection of electrons on the upper subband is provided from the subband 1 by tunnel coupling, while the extraction passes from the lower subband 3 to the subband 4. The transition from the subband 4 to the subband 1′ in the injector involves the emission of LO phonons with energy E_{phon}. The design provides such combination of oscillator strengths Ω_{ij} for diagonal transition in the active region and rates of phonon-assisted scatterings in the injector that a large inversion of populations between lasing states is maintained ensuring large emission power.

2.4. QCL as THz amplifiers

In Ref. [34], a new approach to the generation of high-power broadband THz pulses has been proposed exploiting the effect of the material gain. According to this work, a semiconductor quantum-cascade structure can be used to amplify THz pulses generated via conventional photoconductive antennas. To provide sufficient amplification of THz-pulsed radiation, a quantum-cascade structure should have a large gain coefficient, whose value is generally limited by the gain clamping effect. To overcome this limitation, ultrafast switching of the material gain has been used. The gain coefficient is increased for a short time interval while the input THz pulse is propagating through a QCS. The modulation is implemented using an Auston switch.

In Ref. [35], *by* a series of numerical simulations based on the density matrix formalism, authors have demonstrated that, instead of using the Auston switch, a large instant gain coefficient can be achieved in QCLs by a direct exposition of the structure by ultra-short optical pulses (see **Figure 4(a)**).

The optical pulse is applied to the three-well QCL operating in the pre-threshold regime. As illustrated in **Figure 4(b)**, the design exploits the valance band to provide an interband pumping of electrons into the conduction band. As a result the considered three-well GaAs/AlGaAs QCL demonstrates THz gain increasing up to an order of magnitude under pumping by 100 fs optical pulses with the intensity of 100 MW/cm^2. The gain switching process is characterized by 1 ps rise time and 8 ps recovery time.

The emission spectra from QCL are narrow-band. Therefore, in order to apply them in the THz spectroscopy, one should either make the lasers frequency-tunable or extend their gain/emission spectral band. In the first case, a wideband frequency tuning in QCL can be achieved using a MEMS-based movable silicon plunger [36, 37]. A solution for the second case relies on a multi-stack QCL [38]. The spectral gain of the multi-stack terahertz QCL, composed of three active regions with emission frequencies centered at 2.3, 2.7, and 3.0 THz, is characterized by spectral gain full width at half-maximum of 1.1 THz. Bandwidth and spectral position of the measured gain match with the broadband laser emission. As the laser action ceases with increasing operating temperature, the gain at the dominant lasing frequency of 2.65 THz degrades sharply.

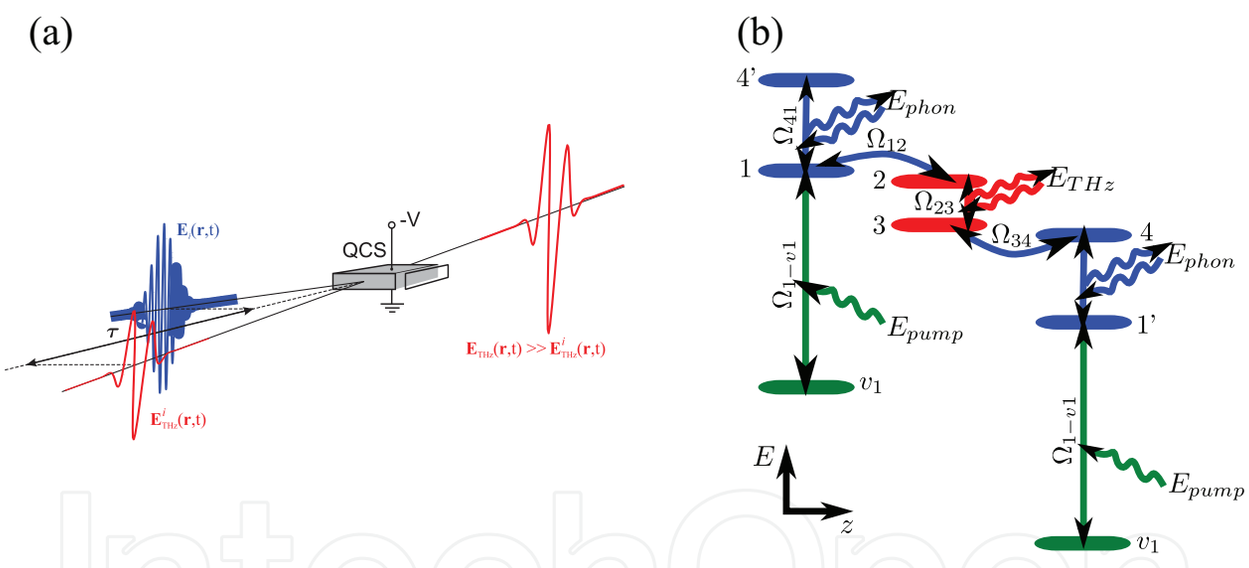

Figure 4. (a) Schematic diagram of the gain switching via ultrafast interband optical pumping and (b) energy versus coordinate structure of the subband edges in the three-well QCL with interband optical pump for gain switching.

3. THz spectroscopy of CBRNE agents

3.1. THz-TDS setups

In **Figure 5**, we show a typical experimental THz-TDS setup with the GaAs photoconductive antenna operating as a THz emitter. The THz-TDS setup starts with a femtosecond laser producing an optical-pulse train. Each pulse separates into two paths. One reaches the THz

http://dx.doi.org/10.5772/67625

emitter where the optical pulses are transformed into ultrashort electromagnetic pulses. The THz pulse then propagates in free space and is focused onto an ultrafast detector. The other part of the pulse is also delivered onto the detector after passing through a time-delay stage. The detector measures the electric-field amplitude of the electromagnetic waves. Although the experimental details vary between different systems, in this example taken from Ref. [6], the emitter contains two vacuum-evaporated NiCr/Au electrodes separated by a submillimeter-wide gap. The electrodes are placed on a doped 1 μm-thick GaAs layer grown on an undoped GaAs substrate. A bias voltage applied across the electrodes changes around ±100 V, modulated at a few kilohertz. The pumping fs pulse generated by Ti:sapphire laser is typically of a few hundred milliwatts average power (~10–100 fs pulse width, 800 nm center wavelength). In this arrangement, a bandwidth of THz pulses is extended up to 3 THz. In an alternative arrangement, the THz radiation is collected "backwards" (in the direction of the reflected pump laser beam). As a result, the absorption and dispersion of the THz pulses in the substrate are minimized that enhances the bandwidth up to 20–25 THz [39]. The emitted THz pulses are collimated and focused onto the sample by a pair of parabolic mirrors. Samples can be scanned across the focus to build a two-dimensional image, each pixel contains spectral information.

There are several ways to provide a coherent detection of the transmitted or reflected THz radiation. Most common technique is based on the ultrafast Pockels effect, where the THz radiation is collected by an electro-optical crystal, for example, ZnTe [40, 41]. The THz field induces an instantaneous birefringence in the electro-optic medium, which is probed with a second visible or near-IR laser beam. Such a beam is split from the pump source. The birefringence modulates the ellipticity of the probe and is detected by a setup consisting of $\lambda/4$ waveplate, a Wollaston prism, and two balanced photodiodes. Also, a lock-in technique can be used to measure a signal from the photodiode using the modulated bias field of the

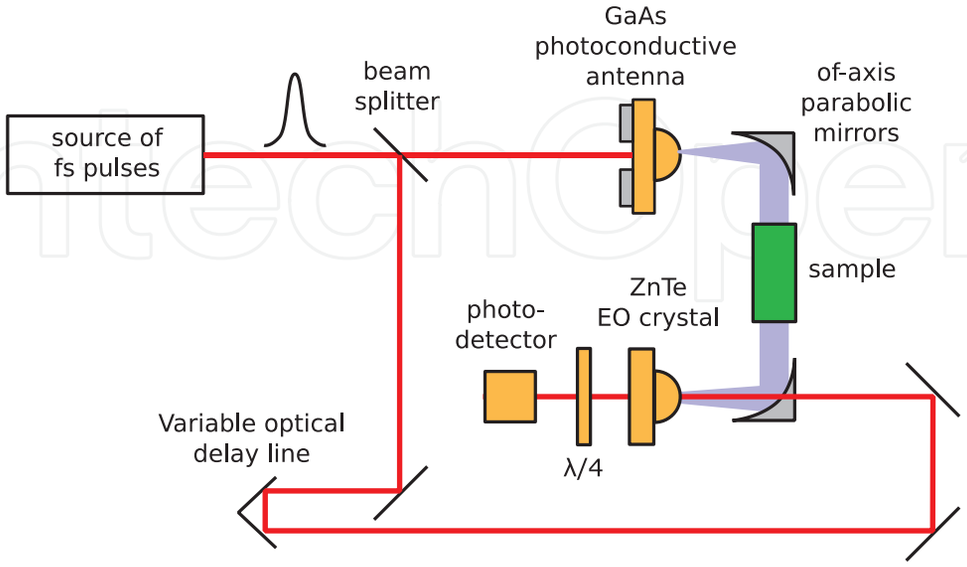

Figure 5. Schematic of a THz-TDS setup.

photoconductive emitter as a reference. In order to obtain the electric field in the time domain, one measures the signal as a function of the time delay between the THz pulse and probe pulses at the electro-optic crystal using a variable delay line. The frequency spectrum of the THz radiation is then obtained by the Fourier transform.

To demonstrate significantly higher spectral resolution and ability to resolve closely spaced lines, the sample may be placed in a parallel plate waveguide with a subwavelength gap between the two plates [42]. Here, a polycrystalline film of a target analyte is formed on one of the inner surfaces of the waveguide plate. The confinement of THz waves ($\lambda/6$ for a typical 50 micron gap) together with a long interaction pathlength (~2–3 cm) allows the THz response of the film to be measured in a sensitive manner over a broad bandwidth from 0.2 to 4 THz. A key idea here is that using relatively simple film formation methods, it is possible to form a highly crystalline quality thin film, which minimizes inhomogeneous line broadening that plagues traditional THz sample preparation methods such as pellet formation. That leads to the resolution of fingerprint lines in threat solids, which are not observed in the conventional free space THz spectroscopy of corresponding pellet samples.

3.2. Explosive materials and their THz spectra

THz-TDS has been shown to be a particularly sensitive technique for studying the structural dynamics of crystal forms, providing additional information for sample analysis. This spectroscopy technique can provide a spectral information being complementary to Raman spectroscopy, owing to the different selection rules governing IR and Raman transitions. Despite the relatively similar chemical structure, the THz frequency spectra are clearly distinct. THz-TDS dominates over other spectroscopic far-IR techniques, such as Fourier transform infrared spectroscopy, since it is insensitive to the thermal background (and hence benefits from a high signal-to-noise ratio). Also, THz-TDS does not require a cryogenically cooled bolometer detector. Another benefit of THz-TDS follows from the fact that both the absorption coefficient and refractive index can directly be extracted without requiring a Kramers-Kronig analysis.

One of the most attractive features of THz spectroscopy is that the THz radiation can penetrate though many nonmetallic and nonpolar materials. This allows to provide spectral analysis of materials concealed within dry packaging, such as paper, natural and synthetic fabrics, plastics, that enables imaging of concealed metallic objects.

First systematic experimental data on THz spectra of a wide range of explosives have been reported by in Ref. [43] and overviewed in Ref. [2]. Their spectra covered the frequency range 0.1–2.8 THz. Later in Ref. [3], the spectroscopic measurements have been extended up to 6 THz (see **Figure 6**). Although many explosives have distinct vibrational absorption features at room temperature, these absorption features tend to be rather broad and overlapping with Q factors ($f/\Delta f$) is less than 10. The broad absorption features are caused by the homogeneous and inhomogeneous line broadening. The resolution of the underlying THz resonances of an explosives solid is a challenging problem and is necessary to achieve a full understanding of the THz properties of molecules of explosives.

http://dx.doi.org/10.5772/67625

Up to date, a wide range of explosive materials have been investigated by THz-TDS, including both pure explosive compounds and plastic explosives, including explosive compounds and mixtures combined with a variety of plasticizers, desensitizers, dyes, waterproof coatings, and fabrics to aid storage and use. All these adulterants may potentially have their own spectral signatures in the THz region, complicating or obscuring the analysis. The pure explosive materials, whose THz spectra are well studied, include ammonium nitrate 2,4,6-trinitrotoluene (TNT) and its degradation product 2,4-dinitrotoluene, 1,3,5,7-tetranitro-1,3,5,7-tetrazocane (HMX), 1,3,5-trinitroperhydro-1,3,5-triazine (RDX), and 1,3-dinitrato-2,2-bis(nitratomethyl)propane (PETN). A comprehensive overview of the THz spectra of a wide range of explosive materials can be found in Ref. [2]. Studies of the plastic explosives Metabel (PETN-based), SX2 (RDX-based), C-4 (RDX-based), PBX (predominantly containing HMX), and Semtex-H (containing both RDX and PETN) have also been reported [44–46]. Most of these studies have focused on THz transmission spectroscopy, as this allows extraction of the absorption coefficient and refractive index of the sample, and the sample thickness/dilution can be optimized to maximize the measurement signal-to-noise ratio. However, there is growing interest in developing THz reflection spectroscopy geometries (both specular and diffuse), as this may be more natural arrangement for standoff detection.

RDX possesses an unusual six-membered heterocyclic ring comprising three nitrogen and three methylene groups, with a nitrite group attached to each of the nitrogen atoms in the ring. This high nitrogen and oxygen content causes explosive properties of this material. A typical THz-TDS spectrum of RDX is shown in **Figure 6(b)**. RDX has a number of characteristic absorption features. The sensing of RDX through covering materials such as plastic, leather, and cotton has been investigated in Ref. [2]; the same has been done using a reflection geometry [47]. In both cases, the spectral features of RDX (especially the absorption peak at 0.8 THz) can be identified. The HMX spectrum (see **Figure 6(a)**) exhibits spectral features below 3 THz, which concur with previously published work and additionally shows six features between 3 and 5 THz. The features between 3 and 5 THz are distinctly different from those present in RDX, allowing improved spectral identification. The data for HMX samples in the 5–6 THz range also have several spectral features; however, they are placed very close to each other [3]. PETN is more sensitive to shock or friction than RDX (or TNT) and is also an extremely powerful explosive. Its THz spectra has two broad bands between 1.5 and 2.5 THz and between 2.5 and 3.5 THz [3]. The TNT spectrum (see **Figure 6(b)**) has a feature near 2 THz as well as an increase in absorption with increasing frequency in the 0.5–3 THz range [3, 43]. Above 3 THz, there are also several significant features.

Most explosive materials are not used in their pure molecular crystalline form, but are mixed with other agents to make plastic explosives such as SX2, Semtex, and Metabel. Metabel shares three absorption features with PETN as well as contributions from each other compound. Also, one observes a clear correspondence between the features of the SX2 spectra and its constituent component RDX. Semtex consists of both RDX and PETN. Comparison of the spectrum of Semtex with those of its components shows a correspondence in a number of peaks): peaks in the Semtex spectrum are caused by a contribution from vibrational modes of

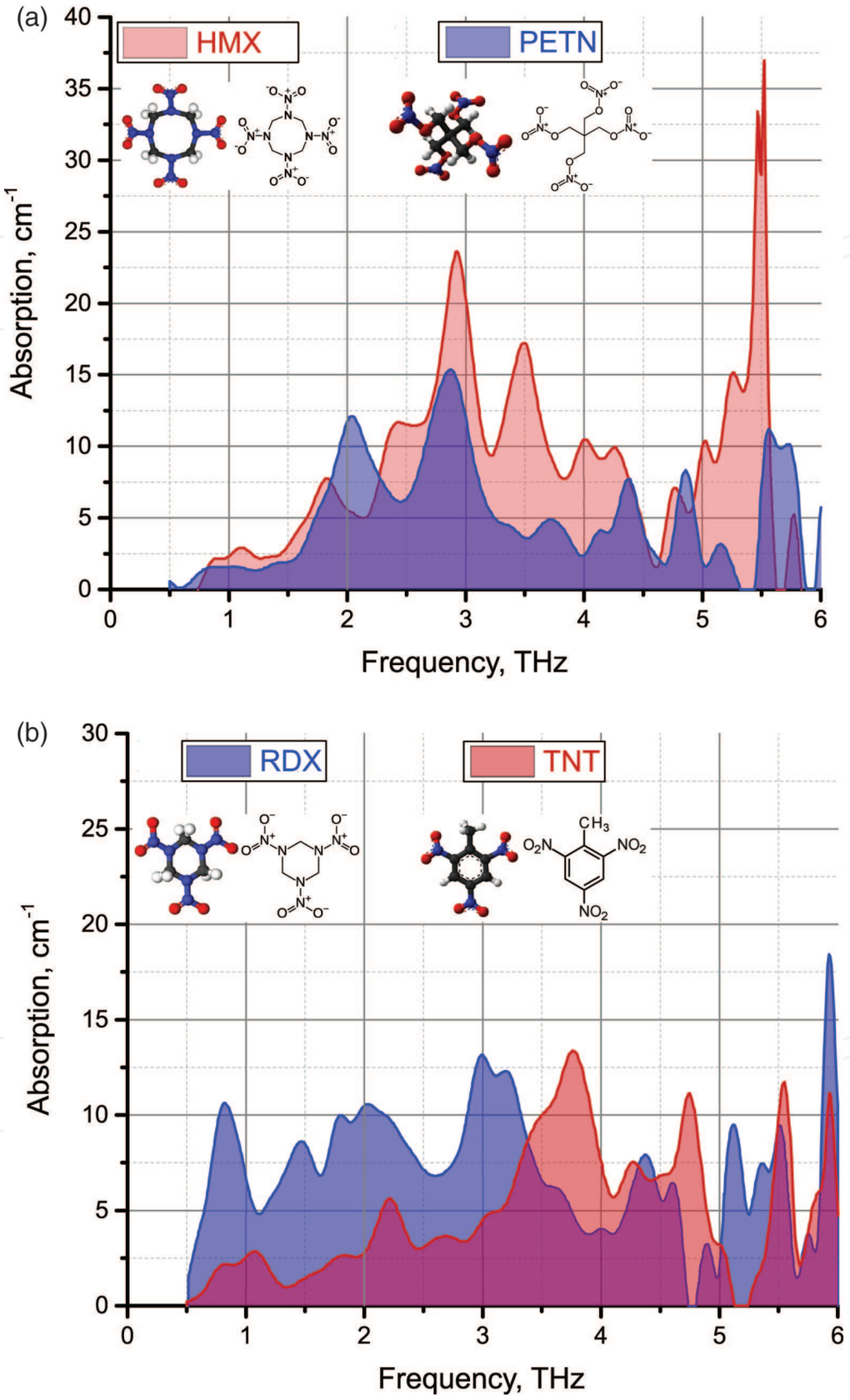

Figure 6. THz absorption spectra of the explosives HMX, PETN, RDX and TNT (the results are adopted from [3]). The chemical structures of the explosives are also shown.

http://dx.doi.org/10.5772/67625

both RDX and PETN, as well as a number of other components. In general, the spectra of the plastic explosives are dominated by the signatures arising from their constituent explosives.

4. Summary

In summary, THz radiation possesses a set of attractive unique features, such as absorption with strongly non-uniform spectral characteristics in most of CBRNE agents, ability to penetrate through many dielectric materials, and nonionizing effect on organic matter. All these features have induced fast recent development of the hardware for THz spectroscopy, including both THz sources and detectors. The photoconductive antennas are most promising sources for the THz time domain spectroscopy. The THz quantum-cascade lasers and emitter based on photomixing phenomena seem to be the best candidates for the coherent broadband continuous-wave terahertz spectroscopy. The quantum-cascade lasers are more compact and produce higher power (tens of miliwatt in low-temperature regime). However, the output power drops with increasing of temperature. Recent developments in the field [31] evidence that the quantum cascade laser can produce a detectable power of several miliwatt at the temperature of 199.5 K. Also, they can be spectral-tunable using MEMS-based movable silicon plunger [36, 37]. The emitters based on the photomixing phenomena do not have issues with operating temperature; however, their output power is limited since their operation is based on high-order optical non-linear effects.

Most explosives have very non-uniform and non-monotonic spectral characteristics, which may serve as fingerprint-like markers for their detection. The absorption spectra of a mixture of explosives contain recognizable features of the constituents that allow for the detection of the components of the mixture. Also, their spectroscopic features are not strongly affected by most of the possible dielectric covering materials. Thus, CBRNE agents can be identified through packaging.

Acknowledgements

Partial support from the University of Guanajuato under projects DAIP-1021/2016 and DAIP-932/2016 is greatly acknowledged. OVS conveys his appreciation to Mauro F. Pereira (Sheffield Hallam University, UK) for continuous support and encouragement.

Author details

Mykhailo Klymenko, Oleksiy Shulika* and Igor Sukhoivanov

*Address all correspondence to: oshulika@ugto.mx

Department of Electronic Engineering, Division of Engineering, Campus Irapuato-Salamanca, University of Guanajuato, Mexico

References

[1] http://doh.dc.gov/service/cbrne-chemical-biological-radiological-nuclear-and-explosives

[2] Chen J., Chen Y., Zhao H., Bastiaans J.G., Zhang X.-C. Absorption coefficients of selected explosives and related compounds in the range of 0.1–2.8 THz. Opt. Exp., 15 (19), 12060 (2007)

[3] Leahy-Hoppa M.R., Fitch M.J., Zheng X., Hayden L.M., Osiander R. Wideband terahertz spectroscopy of explosives. Chem. Phys. Lett., 434, 227–230 (2007)

[4] Kemp M.C., Taday P.F., Cole B.E., Cluff J.A., Fitzgerald A.J., Tribe W.R. Security applications of terahertz technology. Proc. SPIE-Int. Soc. Opt. Eng., 5070, 44–52 (2003)

[5] Federici J.F., Schulkin B., Huang F., Gary D., Barat R., Oliveira F., Zimdars D. THz imaging and sensing for security applications: explosives, weapons, and drugs. Semicond. Sci. Technol., 20 (7), S266–S280 (2005)

[6] Davies A.G., Burnett A.D., Fan W., Linfield E.H., Cunningham J.E. Terahertz spectroscopy of explosives and drugs. Mater. Today, 11 (3), 18–26 (2008)

[7] Appleby R., Wallace H.B. Standoff detection of weapons and contraband in the 100 GHz to 1 THz region. IEEE Trans. Antennas Prop., 55, 2944 (2007)

[8] Berry E., et al. Do in vivo terahertz imaging systems comply with safety guidelines? J. Laser Appl., 15, 192 (2003)

[9] Tonouchi M. Cutting-edge terahertz technology. Nat. Photon., 1, 97–105 (2007)

[10] Lee Y.-S. Principles of terahertz science and technology. New York: Springer Science + Business Media; 2009. 340 p. DOI: 10.1007/978-0-387-09540-0

[11] Tani M., Matsuura S., Sakai K., Nakashima S. Emission characteristics of photoconductive antennas based on low-temperature-grown GaAs and semi-insulating GaAs. Appl. Opt., 36 (30), 7853–7859 (1997)

[12] Sakai K. editor. Terahertz optoelectronics (Topics in applied physics, vol. 97). Heidelberg: Springer-Verlag Berlin Heidelberg; 2005. 387 p. DOI: 10.1007/b80319

[13] Cook D.J., Hochstrasser R.M. Intense terahertz pulses by four-wave rectification in air. Opt. Lett., 25, 1210–1212 (2000)

[14] Doany F.E., Grischkowsky D., Chi C.-C. Carrier lifetime versus ion-implantation dose in silicon on sapphire. Appl. Phys. Lett., 50, 460 (1987)

[15] Gupta S., Frankel M.Y., Valdmanis J.A., Whitaker J.F., Mourou G.A. Subpicosecond carrier lifetime in GaAs grown by molecular beam epitaxy at low temperatures. Appl. Phys. Lett., 59, 3276 (1991)

[16] Auston D. H. Ultrafast optoelectronics. In: Kaiser W. editor. Ultrashort laser pulses: generation and applications. 2nd ed. New York: Springer-Verlag Berlin Heidelberg; 1993. p. 183-234. DOI: 10.1007/BFb0070977

[17] Look D.C., Walters D.C., Robinson G.D., Sizelove J.R., Mier M.G., Stutz C.E. Annealing dynamics of molecular-beam epitaxial GaAs grown at 200 °C. J. Appl. Phys., 74, 306 (1993)

[18] Ferguson B., Zhang X.-C. Materials for terahertz science and technology. Nat. Mater., 1, 26–33 (2002)

[19] Zhao G., Schouten R.N., van der Valk N., Wenckebach W.T., Planken P.C.M. Design and performance of a THz emission and detection setup based on a semi-insulating GaAs emitter. Rev. Sci. Instrum., 73, 1715–1719 (2002)

[20] Katzenellenbogen N., Grischkowsky D. Efficient generation of 380 fs pulses of THz radiation by ultrafast laser pulse excitation of a biased metal–semiconductor interface. Appl. Phys. Lett., 58, 222–224 (1991)

[21] Dekorsy T., Auer H., Waschke C., Bakker H.J., Roskos H.G., Kurz H., Wagner V., Grosse P. Emission of submillimeter electromagnetic waves by coherent phonons. Phys. Rev. Lett., 74, 738 (1995)

[22] Kazarinov R.F., Suris R.A. Possibility of amplification of electromagnetic waves in a semiconductor with a superlattice. Fizika i Tekhnika Poluprovodnikov, 5 (4), 797–800 (1971)

[23] Faist J., Capasso F., Sivco D.L., Sirtori C., Hutchinson A.L., Cho A.Y. Quantum-cascade laser. Science, 264 (5158), 553–556 (1994)

[24] Tredicucci A., Köhler R., Mahler L., Beere H.E., Linfield E.H., Ritchie D.A. Terahertz quantum cascade lasers - first demonstration and novel concepts. Semicond. Sci. Technol., 20 (7), S222 (2005)

[25] Williams B.S., Callebaut H., Kumar S., Hu Q. 3.4-THz quantum cascade laser based on longitudinal-optical-phonon scattering for depopulation. Appl. Phys. Lett., 82, 1015 (2003).

[26] Williams B.S., Kumar S., Callebaut H., Hu Q., Reno J.L. Terahertz quantum-cascade laser operating up to 137 K. Appl. Phys. Lett., 83, 5142 (2003)

[27] Kumar S., Williams B.S., Kohen S., Hu Q., Reno J.L. Continuous-wave operation of terahertz quantum-cascade lasers above liquid-nitrogen temperature. Appl. Phys. Lett., 84, 2494 (2004)

[28] Williams B.S., Kumar S., Hu Q., Reno J.L. Operation of terahertz quantum-cascade lasers at 164 K in pulsed mode and at 117 K in continuous-wave mode. Opt. Exp., 13, 3331 (2005)

[29] Luo H., Laframboise S.R., Wasilewski Z.R., Aers G.C., Liu H.C., Cao J.C. Terahertz quantum-cascade lasers based on a three-well active module. Appl. Phys. Lett., 90, 041112 (2007)

[30] Kumar S., Hu Q., Reno J.L. 186 K operation of terahertz quantum-cascade lasers based on a diagonal design. Appl. Phys. Lett., 94, 131105 (2009)

[31] Fathololoumi S., Dupont E., Chan C.W.I., Wasilewski Z.R., Laframboise S.R., Ban D., Mátyás A., Jirauschek C., Hu Q., Liu H.C. Terahertz quantum cascade lasers operating up to ~ 200 K with optimized oscillator strength and improved injection tunneling. Opt. Exp., 20 (4), 3866–3876 (2012)

[32] Vitiello M.S., Scalari G., Williams B., De Natale P. Quantum cascade lasers: 20 years of challenges. Opt. Exp., 23 (4), 5167–5182 (2015)

[33] Ajili L., Scalari G., Hoyler N., Giovannini M., Faist J. InGaAs–AlInAs/InP terahertz quantum cascade laser. Appl. Phys. Lett., 87 (14), 141107–141107 (2005)

[34] Jukam J., Dhillon S.S., Oustinov D., Madeo J., Manquest C., Barbieri S., Sirtori C., Khanna S.P., Linfield E.H., Davies A.G., Tignon J. Terahertz amplifier based on gain switching in a quantum cascade laser. Nat. Photon., 3 (12), 715–719 (2009)

[35] Shulika O.V., Klymenko M.V., Sukhoivanov I.A. Ultrafast interband pumping of quantum-cascade structures: a feasibility study of a THz pulse amplifier. Laser Photon. Rev., 8 (1), 188–195 (2014)

[36] Qin Q., et al. Tuning a terahertz wire laser. Nat. Photon., 3, 732–737 (2009)

[37] Sirtori C., Barbieri S., Colombelli R. Wave engineering with THz quantum cascade lasers. Nat. Photon., 7, 691–701 (2013)

[38] Bachmann D., et al. Spectral gain profile of a multi-stack terahertz quantum cascade laser. Appl. Phys. Lett., 105, 181118 (2014)

[39] Shen, Y.-C., et al. Ultrabroadband terahertz radiation from low-temperature-grown GaAs photoconductive emitters. Appl. Phys. Lett., 83, 3117 (2003)

[40] Wu Q., Zhang X.-C. 7 terahertz broadband GaP electro-optic sensor. Appl. Phys. Lett., 70, 1784 (1997)

[41] Leitenstorfer A., et al. Detectors and sources for ultrabroadband electro-optic sampling: experiment and theory. Appl. Phys. Lett., 74, 1516 (1999)

[42] Theuer M., Sree Harsha S., Grischkowsky D. Flare coupled metal parallel-plate waveguides for high resolution THz time-domain spectroscopy. J. Appl. Phys., 108, 113105, (2010)

[43] Tribe W.R., et al. Hidden object detection: security applications of terahertz technology. Proc. SPIE, 5354, 168 (2004)

[44] Burnett A., et al. Broadband terahertz time-domain and Raman spectroscopy of explosives. Proc. SPIE, 6549, 654905 (2007)

[45] Yamamoto K., et al. Noninvasive inspection of C-4 explosive in mails by terahertz time-domain spectroscopy. Jpn. J. Appl. Phys., 43, L414 (2004)

[46] Funk D.J., et al. THz transmission spectroscopy and imaging: application to the energetic materials PBX 9501 and PBX 9502. Appl. Spectrosc., 58, 428 (2004)

[47] Liu H.-B., et al. Detection and identification of explosive RDX by THz diffuse reflection spectroscopy. Opt. Exp., 14, 415 (2006)